Chemical Science

ROYAL SOCIETY OF CHEMISTRY

EDGE ARTICLE

View Article Online
View Journal | View Issue

Cite this: *Chem. Sci.*, 2026, **17**, 6079

All publication charges for this article have been paid for by the Royal Society of Chemistry

Received 6th December 2025
Accepted 24th January 2026

DOI: 10.1039/d5sc09574c

rsc.li/chemical-science

A molecular dual-center emitter for ratiometric optical thermometry

Rong Sun, †[a] Hong Huang,†[b] Ye Xia,[b] Youchao Liu,[b] Xingquan Tao,[b] Jun-Long Zhang,[a] Bing-Wu Wang *[ac] and Song Gao *[ad]

Ratiometric optical thermometers have attracted significant interest due to their high accuracy, self-referencing capability and strong resistance to environmental fluctuations. However, most reported systems rely on doped materials, where random donor–acceptor distributions and batch-to-batch variability hinder reproducibility and restrict practical deployment for high-precision temperature sensing. Molecular ratiometric thermometers with precisely controlled donor–acceptor distances and fixed stoichiometry serve as promising candidates, yet remain largely unexplored. This work reports a dual-center emissive 3d–4f binuclear complex [ZnLSm(OAc)$(NO_3)_2$] (**ZnSm**), constructed using a Schiff base ligand (L). **ZnSm** exhibits two well-correlated emission bands at 485 nm (ZnL) and 644 nm (Sm^{3+}), enabling quantitative temperature readout over a broad temperature range of 233–333 K with excellent reversibility and a high maximum relative sensitivity of 3.4% K^{-1}. Spectroscopic analyses and theoretical calculations reveal efficient ZnL-to-Sm^{3+} energy transfer mediated by the bridging Schiff base ligand, accounting for the temperature-dependent dual emission. Moreover, **ZnSm** can be readily processed into a transparent and flexible poly(methyl methacrylate) (PMMA) film (**ZnSm@PMMA**) while retaining its ratiometric thermometric performance, thus greatly enhancing its applicability for practical thermal mapping and device-integrated sensing. This work presents a robust molecular design strategy for developing high-performance, dual-center emissive ratiometric optical thermometers. Furthermore, the readily distinguishable color change in the visible range for both **ZnSm** and its film highlights their potential for advanced optical anti-counterfeiting and information encryption applications.

Introduction

High-precision temperature sensing plays a crucial role across various scientific and technological domains,[1] spanning chemical reaction regulation,[2] thermal management in microdevices,[3–5] and biological process monitoring.[6–11] Even subtle local temperature fluctuations, as small as 1–2 °C, can profoundly influence critical phenomena such as phase transitions and cellular metabolic activities.[6,12] Consequently, developing techniques capable of rapid, accurate, and non-contact temperature detection that can meet the challenges posed by increasingly miniaturized scales and fast dynamic processes is essential for advancing our ability to understand and control complex systems. Despite the availability of conventional thermometers such as thermocouples and resistance temperature detectors, they remain inadequate for emerging applications that require spatially resolved or time-resolved temperature mapping.[13,14] Also, their physical contact with targets limits usability in corrosive environments or living organisms.

To address these challenges, optical thermometry,[15–20] which harnesses the temperature-dependent photophysical response of a probe, has emerged as a leading approach due to its remote, non-contact nature, high sensitivity, and high-resolution imaging capabilities. It principally employs two main strategies: tracking temperature-induced changes in either luminescence lifetimes or emission intensities.[15] Early optical thermometers primarily relied on the absolute change of emission intensity with temperature. However, such single-intensity-based methods suffer from poor reliability due to fluctuations in excitation power, probe concentration and optical path. Alternatively, lifetime-based methods can offer high sensitivity,[15,21,22] but their implementation is highly technically demanding. More importantly, this technique is inherently limited for dynamic measurements that fall within or below the probe's lifetime,[23] making it ineffective for rapid

[a]*Beijing National Laboratory for Molecular Sciences, College of Chemistry and Molecular Engineering, Peking University, Beijing, 100871, P. R. China. E-mail: wangbw@pku.edu.cn; gaosong@pku.edu.cn*

[b]*Spin-X Institute, School of Chemistry and Chemical Engineering, South China University of Technology, Guangzhou 510641, P. R. China*

[c]*School of Chemical Engineering, Guizhou Minzu University, Guiyang 550025, P. R. China*

[d]*Guangdong Basic Research Center of Excellence for Functional Molecular Engineering, School of Chemistry, Sun Yat-sen University, Guangzhou, 510275, P. R. China*

† These authors contributed equally to this work.

thermal mapping. In this context, ratiometric intensity-based thermometry presents a compelling alternative by correlating temperature with the intensity ratio of two distinct emission bands.[24] This ratiometric approach inherently eliminates the necessity of additional intensity calibration and mitigates signal interference from both environmental changes and instrumental fluctuations, ultimately leading to enhanced accuracy and high stability.

Rare-earth-based thermometry[17] is highly appealing due to the unique luminescent properties of the shielded 4f orbitals,[25,26] including long luminescence lifetimes,[27] as well as narrow emission peaks at well-defined positions that can be easily distinguished from background fluorescence.[28] Multiple rare-earth luminescent materials have been developed for temperature detection,[17,29–38] primarily based on the doping method. However, achieving identical concentration and quality across different batches of doped materials is challenging. Furthermore, the efficiency of energy transfer critically depends on the donor–acceptor distance, which is inherently random in doped systems and can only be treated statistically.[39] These limitations reduce the accuracy of the resulting thermometers and greatly constrain their practical application as high-precision temperature sensors. In contrast, molecular complexes offer a highly promising strategy due to their precise synthesis, ease of modulation and suitability for large-scale production. Among them, molecular complexes featuring dual emission centers have emerged as a particularly compelling yet largely unexplored strategy. In particular, heterometallic architectures provide precisely defined spatial arrangements of the ligand antenna and rare-earth emitter, together with fixed stoichiometric ratios, enabling controllable and reproducible energy transfer efficiencies[40] that are highly advantageous for constructing ratiometric optical thermometers. Moreover, the structural and photophysical tunability of these complexes provides a versatile platform for tailoring their emission characteristics.

Here, we present such a class of dual-center emissive complex [ZnLSm(OAc)$(NO_3)_2$] (**ZnSm**, 1*R*,2*R*-H_2L = [6,6′-((1*E*,1′*E*)-(((1*R*,2*R*)-1,2-diphenylethane-1,2-diyl)bis(azaneylylidene))bis(-methaneylidene))bis(2-methoxyphenol)]), constructed using a Schiff base ligand as the bridging unit. **ZnSm** exhibits characteristic narrow emissions of Sm^{3+} (560, 599 and 644 nm), along with a broad emission centered at 485 nm originating from the ZnL moiety. Notably, the intensity ratio between the red emission at 644 nm and the blue emission at 485 nm shows pronounced temperature dependence over a wide range of 233–333 K, with a maximum relative sensitivity of 3.4% K^{-1}, making it suitable for constructing high-performance ratiometric optical thermometers with excellent stability and reversibility. To the best of our knowledge, such a high relative sensitivity ranks among the highest reported to date for ratiometric luminescent thermometers. Importantly, this temperature range covers the physiological window, rendering **ZnSm** particularly attractive to bio-related thermal monitoring,[10,18] such as cell or tissue temperature tracking, and thermal control in microfluidic bioreaction systems. Additionally, its temperature-responsive emission color change can be utilized as a trigger for optical anti-counterfeiting and information encryption.[41–43] Combined experimental and theoretical investigations indicate that the triplet state of the bridging Schiff base ligand plays a crucial role in the energy transfer process, with its energy level well-matched to the Sm^{3+} excited state, thereby facilitating well-correlated dual-emission response. Furthermore, **ZnSm** can be readily processed into a transparent and flexible poly(methyl methacrylate) (PMMA) film while retaining its ratiometric thermometric performance, greatly enhancing its practicality for device integration.[44] By constructing such a dinuclear complex, this work successfully achieves temperature-dependent dual-center emission. Compared with single-center molecular ratiometric optical thermometers and doped materials, such dual-center emissive systems provide greater structural tunability, enhanced opportunities for performance optimization and higher measurement reliability, shedding light on the design of high-performance ratiometric optical thermometers.

Results and discussion

Synthesis and crystal structures

Schiff base ligand 1*R*,2*R*-H_2L (SI Scheme S1), zinc(II) acetate [$Zn(OAc)_2\cdot 2H_2O$] and samarium(III) nitrate [$Sm(NO_3)_3\cdot 5H_2O$] were dissolved in methanol and heated to 75 °C overnight, yielding **ZnSm** crystals suitable for X-ray crystallography on the inner walls of the sealed vessel. Single-crystal X-ray analysis performed at 150 K reveals that **ZnSm** crystallizes in the polar space group $P2_1$ with two crystallographically independent heteronuclear complexes (Zn1Sm1 and Zn2Sm2) within an asymmetric unit (Fig. 1a, Tables S1 and S2). In the complex, the phenolate ions from the Schiff base ligand together with the acetate ligand bridge the Zn^{2+} and Sm^{3+} ions, giving Zn1–Sm1 and Zn2–Sm2 distances of 3.365(14) Å and 3.373(14) Å, respectively. The Zn^{2+} center is embedded within the inner N_2O_2 coordination pocket of the Schiff base ligand, whereas the Sm^{3+} ion is bound by the external phenoxo/methoxy O_2O_2 donors and two additional nitrate ions. The Sm–O bonds range from 2.329(10) to 2.632(10) Å, while the Zn–O bonds are significantly shorter, in the range of 1.971(9)–2.014(8) Å. The large steric hindrance of the chelating Schiff base ligand effectively separates the molecules in the crystal lattice. The shortest intermolecular metal–metal distance is the Zn1···Zn2 separation of 7.2600(19) Å, while the shortest Sm···Sm and Zn···Sm distances

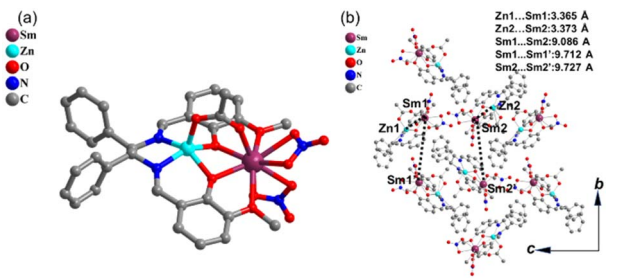

Fig. 1 Molecular structure of **ZnSm**. (a) One of the crystallographically independent heteronuclear units. (b) View of the packing arrangement along the crystallographic *a* axis.

are 9.0876(8) and 9.0820(14) Å (Fig. 1b), respectively. No significant intermolecular interactions such as hydrogen bonding or π···π stacking are observed in the crystal packing. Additionally, an isostructural complex, [ZnLGd(OAc)$(NO_3)_2$] (**ZnGd**, Fig. S10), was prepared following similar synthetic procedures as a reference to help elucidate the temperature-dependent dual-emission behavior in **ZnSm**.

Photophysical properties

The powder X-ray diffraction (PXRD) patterns of **ZnSm** are well indexed and in excellent agreement with simulations based on single-crystal data, confirming its phase purity (Fig. S1). Thermogravimetric analysis (TGA) demonstrates the thermal stability of **ZnSm**, which remains stable up to 573 K. As shown in Fig. S2, the absence of significant mass loss prior to decomposition confirms the solvent-free nature of the lattice. Furthermore, differential scanning calorimetry (DSC) measurements conducted between 293 and 573 K reveal no evidence of structural phase transitions before the compound decomposes (Fig. S3). The excitation and emission spectra of **ZnSm** were first collected at room temperature in both solution and solid states (Fig. S4–S7). Upon excitation at 365 nm, four distinct emission peaks are clearly observed for **ZnSm** in both solution (485, 560, 599, and 644 nm) and the solid state (468, 560, 599, and 644 nm). The overall spectral profiles are highly similar, with three emission peaks appearing at identical wavelengths and only a slight red shift of the high-energy band in solution, which indicates that the overall coordination environment of **ZnSm** is largely retained in solution and that no significant metal scrambling occurs. The narrow emission peaks at 560, 599, and 644 nm are assigned to characteristic transitions ($^4G_{5/2} \rightarrow {}^6H_J$, J = 5/2, 7/2, 9/2) of Sm^{3+},[45] while the much broader blue emission at 485 nm is tentatively attributed to the luminescence of the ZnL moiety.[46] Given that the electronic excited states of Gd^{3+} are very high and that it is typically emission-silent, the spectra of **ZnGd** were collected to aid the assignment of the 485 nm emission peak in **ZnSm**. Notably, the broad blue emission is still observed in **ZnGd** (Fig. S11), confirming that it originates from the ZnL moiety rather than the rare-earth ion.

Motivated by the above dual-center emission behavior observed at room temperature, we then investigated the temperature-dependent photoluminescent (PL) properties of **ZnSm** to evaluate its potential as a ratiometric optical thermometer. As shown in Fig. 2a, the emission intensity at 485 nm of ZnL decreases substantially due to the thermal activation of nonradiative decay pathways, whereas the intensity of Sm^{3+} $^4G_{5/2} \rightarrow {}^6H_{9/2}$ transition at 644 nm increases with rising temperature in the range of 233–333 K. This temperature-dependent PL behavior may arise from the energy transfer from ZnL to Sm^{3+} ions *via* the bridging ligands, and the underlying mechanism is explored (*vide infra*). Strikingly, the luminescent color of **ZnSm** gradually changes from green to orange-red and finally to red when it is irradiated with UV light as the temperature is raised from 233 to 333 K, as shown in Fig. 2b. This reversible and visually distinguishable luminescent color change within a practical temperature range enables potential applications in advanced optical anti-counterfeiting and information encryption.[41]

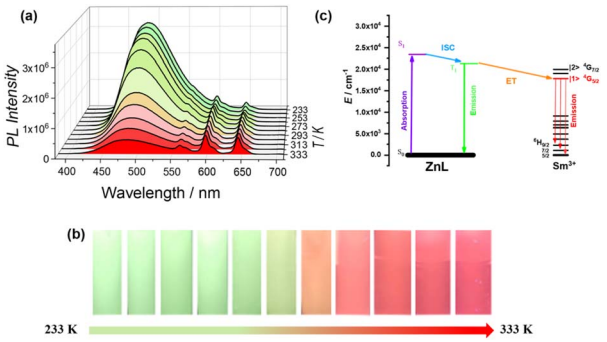

Fig. 2 Temperature dependence of emission properties for **ZnSm**. (a) Emission spectra in toluene (1.0×10^{-5} M) between 233 and 333 K under 365 nm excitation. (b) The luminescent color change at different temperatures (233–333 K, toluene solution). (c) Relative energy levels and possible energy transfer (ET) pathway.

Theoretical calculations were performed to elucidate the electronic structures and the origin of the temperature-dependent dual-emission behavior of **ZnSm**. The calculated relative energy levels of the ZnL moiety and Sm^{3+} ion (Tables S4–S6), along with the possible energy-transfer pathway, are illustrated in Fig. 2c. The triplet excited (T_1) state of the ZnL moiety is located at 20 595 cm^{-1} (485.6 nm), consistent with the observed broad blue emission. In contrast, the energy separation between the singlet excited (S_1) and ground state (S_0) is 28 418 cm^{-1} (351.9 nm), which is much larger, indicating that the short-wavelength emission originates from the transition from the T_1 to S_0 state. This assignment is further supported by the long lifetime (~μs) of the 485 nm emission. Electronic structure calculations of Sm^{3+} reveal that the low-lying multiplet ^6H_J (J = 5/2, 7/2, 9/2) states are located at 0–324, 1117–1499, and 2459–2808 cm^{-1}, respectively, whereas the excited $^4G_{5/2}$ state lies in the range of 18 665–19 607 cm^{-1}. These calculated energy levels agree well with the experimentally observed emission bands, corresponding to transitions from the lowest M_J sublevel of the $^4G_{5/2}$ excited state to the respective ^6H_J (J = 5/2, 7/2, 9/2) states. Importantly, the small energy gap between the T_1 state of the ZnL moiety and the $^4G_{5/2}$ state of Sm^{3+} (~2200 cm^{-1}) favors thermally assisted ZnL-to-Sm^{3+} energy transfer, whereas the much larger T_1–S_1 gap (7823 cm^{-1}) renders reverse intersystem crossing (rISC) inefficient. Upon heating, thermal activation enhances the population of the ZnL T_1 state, thereby facilitating energy transfer to the Sm^{3+} $^4G_{5/2}$ state and resulting in the intensified 644 nm emission. Furthermore, the T_1 spin density is predominantly localized on the bridging Schiff base ligand (Table S7), mainly distributed around the bridging oxygen atoms that coordinate directly to Sm^{3+}. This proximate localization, together with the short O–Sm distance (~2.4 Å) imposed by the coordination geometry, provides a favorable orbital-overlap pathway for efficient intramolecular Dexter-type energy transfer. Collectively, the thermally enhanced energy transfer strengthens the long-wavelength Sm^{3+} emission while suppressing ZnL emission, giving rise to a distinct and reversible luminescent color evolution.

Such an energy-transfer process was further verified by temperature-dependent lifetime measurements (Fig. S8 and S9). The lifetime of the Sm^{3+} $^4G_{5/2} \rightarrow {}^6H_{9/2}$ transition at 644 nm increases to 50.6 μs at 333 K, representing a 20% enhancement compared with that at 233 K. In contrast, the emission lifetime of the ZnL moiety at 485 nm decreases by nearly 5% over the same temperature range, indicating that the ZnL T_1 state is increasingly depopulated through thermally enhanced energy transfer to Sm^{3+}, with nonradiative thermal quenching also involved. These opposite lifetime changes confirm that the temperature-dependent dual-center emissive behavior of **ZnSm** benefits from the ZnL-to-Sm^{3+} energy transfer process.

Ratiometric thermometry of ZnSm

To evaluate the ratiometric thermometric performance of **ZnSm**, the temperature-dependent luminescence intensities were investigated. As shown in Fig. 3a, the emission band of the ZnL moiety at 485 nm is significantly quenched, decreasing by 85.3% as the temperature increases from 233 to 333 K. In contrast, the characteristic Sm^{3+} emission at 644 nm nearly doubles in intensity over the same temperature range. This opposite intensity evolution enables temperature readout through the emission intensity ratio. A good linear correlation is observed between temperature and the natural logarithm of the intensity ratio of Sm^{3+} (644 nm) to ZnL (485 nm), $\ln(I_{644}/I_{485})$, as illustrated in Fig. 3b. The correlation can be expressed using eqn (1):

$$\ln(I_{644}/I_{485}) = 0.03186T - 10.4888 \quad (1)$$

where I_{644} and I_{485} represent the emission intensities of Sm^{3+} and ZnL at 644 and 485 nm, respectively, and T is the absolute temperature in Kelvin. The excellent linearity, evidenced by a correlation coefficient $R^2 = 0.9966$ (253–333 K), confirms the reliability of the ratiometric calibration. The reversibility of **ZnSm** was further evaluated by repeatedly cycling the temperature between 233 and 333 K over six consecutive runs (Fig. 3c). The intensity ratios recorded at the same temperature across different cycles remain almost unchanged, demonstrating the excellent thermal stability and reversibility of the sensing performance. These results highlight **ZnSm** as a promising self-referencing molecular optical thermometer.

Sensitivity is a key figure of merit for temperature sensors, and a proper sensitivity metric is essential for evaluating and comparing different thermometric systems. To enable quantitative comparison across thermometers operating *via* different mechanisms, the relative sensitivity (S_r) is commonly employed.[47–50] For **ZnSm**, S_r can be calculated according to eqn (2):

$$S_r(T) = (\partial(I_{644}/I_{485})/\partial T)/(I_{644}/I_{485}) \quad (2)$$

As shown in Fig. 3d, **ZnSm** retains high sensitivity ($S_r > 1\%$ K^{-1}) within the broad temperature range of 253–333 K when measured at a concentration of 1.0×10^{-5} M, reaching a maximum value of 3.4% K^{-1} at 333 K when measured at a concentration of 1.0×10^{-5} M, which ranks among the highest so far for ratiometric luminescent thermometers (Table S8). Such a wide operating range combined with outstanding sensitivity meets the criteria of good-performance thermometry.

Beyond conventional doped luminescent thermometers, **ZnSm** integrates two emissive centers, ZnL and Sm^{3+}, within a single, well-defined molecular framework through deliberate molecular design. This binuclear architecture enables stable, highly sensitive, and reproducible temperature-dependent dual-emission behavior. Owing to the shielded nature of 4f orbitals, the f–f emission of Sm^{3+} exhibits fixed positions, narrow linewidths, and long-wavelength characteristics, whereas the ligand-centered ZnL emission is located in the short-wavelength region. Such intrinsic differences in emission origin and spectral position effectively minimize spectral overlap between the two emissive bands, allowing clear peak discrimination and accurate determination of emission intensity ratios, which is critical for achieving high relative thermal sensitivity. In addition, many ratiometric thermometers are constructed based on a single emissive center, particularly those exploiting the fine structure of excited- and/or ground-state multiplets of rare-earth ions to generate so-called "hot" and "cold" emission bands.[37,38] In these systems, the operational temperature range and sensitivity are largely dictated by crystal-field splitting and the energy gaps between Stark sublevels. While this approach has proven effective, precise modulation of excited states in rare-earth ions remains challenging due to the inherently rigid nature of the 4f electronic structure, which can limit further sensitivity enhancement and flexible tuning of the working temperature window. In this context, the dual-center molecular strategy employed in **ZnSm** provides a versatile alternative. Guided by the Dieke diagram, the excited-state energetics and emission behavior of rare-earth ions can be rationally anticipated. By pairing rare-earth ions with organic ligands possessing appropriately matched triplet energy levels and enforcing fixed donor–acceptor distances through tailored coordination architectures,

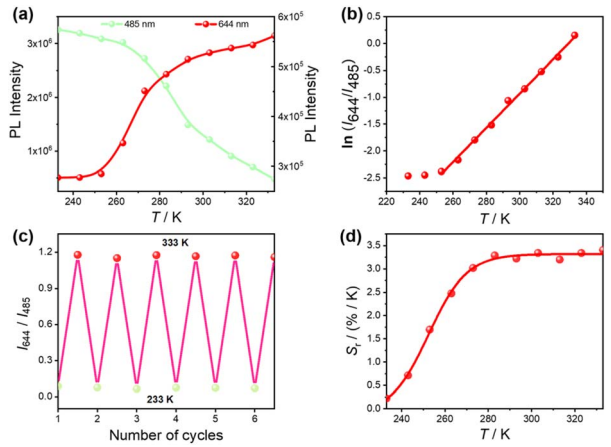

Fig. 3 Ratiometric thermometric performance of **ZnSm**. (a) Temperature-dependent emission intensities of the ZnL band (485 nm) and Sm^{3+} band (644 nm). (b) Temperature-dependence of the intensity ratio (I_{644}/I_{485}). The red line represents the fitting results using eqn (1). (c) Reversibility of I_{644}/I_{485} over six heating–cooling cycles between 233 and 333 K. (d) Temperature-dependent relative sensitivity (S_r). The solid line serves as a guide for the eye.

property-tunable dual-center emitters for ratiometric thermometers can be constructed.

Ratiometric thermometry of ZnSm@PMMA

Encouraged by the wide operating temperature range, high relative sensitivity, and excellent reversibility of **ZnSm**, we further explored its applicability in device-compatible formats. PMMA was selected as a polymer host owing to its high transparency, mechanical flexibility, environmental stability, and biocompatibility. Incorporation of **ZnSm** into PMMA was readily achieved through a simple hybrid fabrication process, yielding a transparent and ductile **ZnSm@PMMA** film (Fig. 4a). To assess its capability as a flexible luminescent thermometer, the temperature-dependent emission behavior of the **ZnSm@PMMA** film was systematically examined (Fig. S12). The film maintains the characteristic dual-center emission (Fig. S13 and S14) and exhibits temperature-dependent luminescent evolution similar to that observed in the pristine complex. Furthermore, a good linear correlation is also observed between temperature and the natural logarithm of the intensity ratio $\ln(I_{644}/I_{485})$ (Fig. 4b), which can be expressed using eqn (3):

$$\ln(I_{644}/I_{485}) = 0.0044T - 1.0986 \quad (3)$$

with a correlation coefficient of 0.9856. Based on eqn (3), the maximum relative sensitivity of the **ZnSm@PMMA** film is deduced to be 0.57% K^{-1} at 333 K (Fig. 4c), which is comparable to those of the previously reported doped metal–organic framework (MOF)-based optical thermometers.[51,52]

The macroscopic and reversible luminescent color variation is conducive to intuitive temperature readout without the need of specialized instrumentation such as fluorescence spectrophotometers. The temperature-dependent chromatic evolution of the **ZnSm@PMMA** film was quantitatively illustrated using the Commission International de L'Eclairage (CIE) 1931 coordinates (Fig. S15), showing a continuous shift from green (0.2660, 0.3119) to red (0.2827, 0.2507) upon heating from 233 to 333 K. Thus, the temperature information could also be directly estimated through naked-eye color observation referenced to the corresponding CIE coordinates, offering a convenient and low-cost visualization strategy similar to commercial pH strips. Collectively, the reliable ratiometric response and preserved temperature-sensing performance in flexible film form highlight the strong potential of **ZnSm@PMMA** for practical thermal mapping and on-site temperature diagnostics.

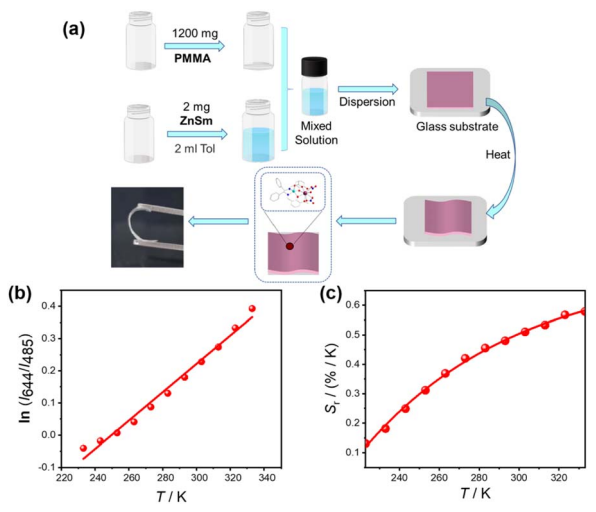

Fig. 4 Preparation and ratiometric thermometric performance of ZnSm@PMMA. (a) Schematic presentation of the preparation process. (b) Temperature-dependence of the intensity ratio (I_{644}/I_{485}). The red line represents the fitting results using eqn (3). (c) Temperature-dependent relative sensitivity (S_r). The solid line serves as a guide for the eye.

Conclusions

In summary, a dual-center emissive heterometallic complex **ZnSm** was successfully constructed using a Schiff base ligand *via* a solution-based synthesis strategy. The temperature-dependent emission analysis reveals that **ZnSm** exhibits reliable ratiometric thermometric behavior over a broad operating range of 233–333 K, achieving a high maximum relative sensitivity of 3.4% K^{-1} with excellent reversibility. Meanwhile, the conspicuous and reversible color transition from green to red provides an intuitive means for visual temperature estimation and offers additional opportunities for optical anti-counterfeiting and information-encryption applications. Combined spectroscopic experiments and theoretical investigations confirm that the favorable ZnL-to-Sm^{3+} energy transfer mediated by the bridging Schiff base ligand is responsible for the well-correlated intensity responses of the two emissive centers. Furthermore, a transparent and flexible **ZnSm@PMMA** film was fabricated, in which the temperature-sensing performance of the pristine complex is preserved, thus greatly enhancing its applicability in practical thermal mapping and device-integrated sensing scenarios. Overall, this work presents a versatile molecular design strategy for developing high-performance ratiometric optical thermometers based on dual-center emissive complexes and opens new avenues toward functional luminescent devices.

Author contributions

All authors have given approval to the final version of the manuscript. CRediT: Rong Sun: investigation, visualization, writing original draft, writing – review & editing; Hong Huang: investigation, visualization, writing original draft, writing – review & editing; Ye Xia: investigation; Youchao Liu: investigation; Xingquan Tao: investigation; Jun-Long Zhang: writing – review; Bing-Wu Wang: funding acquisition, project administration, writing – review & editing; Song Gao: funding acquisition, project administration, writing – review & editing.

Conflicts of interest

H. Huang and S. Gao are the inventors on an authorized patent (Patent No. CN 116284067 B) relating to the preparation of a **ZnSm**-based ratiometric temperature sensor. The authors declare no other competing interests.

Data availability

The supporting data are provided as part of the supplementary information (SI). Supplementary information: experimental details, X-ray crystallography, computational details, and supporting figures and tables. See DOI: https://doi.org/10.1039/d5sc09574c.

CCDC 2270399 for **ZnSm** and 2503173 for **ZnGd** contain the supplementary crystallographic data for this paper.[53a,b]

Acknowledgements

The authors gratefully acknowledge the financial support from the Natural Science Foundation of China (Grant No. 22573003 and 22131003). All the calculations were supported by the High-performance Computing Platform of Peking University.

Notes and references

1 J. Zhou, B. del Rosal, D. Jaque, S. Uchiyama and D. Jin, *Nat. Methods*, 2020, **17**, 967–980.
2 T. Hartman, R. G. Geitenbeek, C. S. Wondergem, W. van der Stam and B. M. Weckhuysen, *ACS Nano*, 2020, **14**, 3725–3735.
3 M. Mecklenburg, W. A. Hubbard, E. R. White, R. Dhall, S. B. Cronin, S. Aloni and B. C. Regan, *Science*, 2015, **347**, 629–632.
4 S. Fujii, Y. Shoji, T. Fukushima and T. Nishino, *J. Am. Chem. Soc.*, 2011, **143**, 18777–18783.
5 Q. Cheng, S. Rajauria, E. Schreck, R. Smith, N. Wang, J. Reiner, Q. Dai and D. Bogy, *Sci. Rep.*, 2020, **10**, 20087.
6 K. Okabe, N. Inada, C. Gota, Y. Harada, T. Funatsu and S. Uchiyama, *Nat. Commun.*, 2012, **3**, 705.
7 G. Kucsko, P. C. Maurer, N. Y. Yao, M. Kubo, H. J. Noh, P. K. Lo, H. Park and M. D. Lukin, *Nature*, 2013, **500**, 54–58.
8 C. W. Chung, A. D. Stephens, T. Konno, E. Ward, E. Avezov, C. F. Kaminski, A. A. Hassanali and G. S. Kaminski Schierle, *J. Am. Chem. Soc.*, 2022, **144**, 10034–10041.
9 M. Quintanilla, M. Henriksen-Lacey, C. Renero-Lecuna and L. M. Liz-Marzán, *Chem. Soc. Rev.*, 2022, **51**, 4223–4242.
10 Y. Xing, J. Cui, N. Nedved, J. A. O'Hara and Y. Yu, *JACS Au*, 2025, **5**, 2939–2952.
11 Y. Lee, K. Kim, D. Kim and J. S. Lee, *J. Am. Chem. Soc.*, 2025, **147**, 13180–13189.
12 M. Preußner, G. Goldammer, A. Neumann, T. Haltenhof, P. Rautenstrauch, M. Müller-McNicoll and F. Heyd, *Mol. Cell*, 2017, **67**, 433–446e4.
13 M. M. Kim, A. Giry, M. Mastiani, G. O. Rodrigues, A. Reis and P. Mandin, *Microelectron. Eng.*, 2015, **148**, 129–142.
14 F. Menges, P. Mensch, H. Schmid, H. Riel, A. Stemmer and B. Gotsmann, *Nat. Commun.*, 2016, **7**, 10874.
15 C. D. S. Brites, P. P. Lima, N. J. O. Silva, A. Millán, V. S. Amaral, F. Palacio and L. D. Carlos, *Nanoscale*, 2012, **4**, 4799–4829.
16 A. Cadiau, C. D. S. Brites, P. M. F. J. Costa, R. A. S. Ferreira, J. Rocha and L. D. Carlos, *ACS Nano*, 2013, **7**, 7213–7218.
17 E. V. Salerno, A. N. Carneiro Neto, S. V. Eliseeva, M. A. Hernández-Rodríguez, J. C. Lutter, T. Lathion, J. W. Kampf, S. Petoud, L. D. Carlos and V. L. Pecoraro, *J. Am. Chem. Soc.*, 2022, **144**, 18259–18271.
18 K. Xue, C. Wang, J. Wang, S. Lv, B. Hao, C. Zhu and B. Z. Tang, *J. Am. Chem. Soc.*, 2021, **143**, 14147–14157.
19 X.-d. Wang, O. S. Wolfbeis and R. J. Meier, *Chem. Soc. Rev.*, 2013, **42**, 7834–7869.
20 D. Li, M. Jia, T. Jia and G. Chen, *Adv. Mater.*, 2024, **36**, 2309452.
21 H. Gao, C. Kam, T. Y. Chou, M.-Y. Wu, X. Zhao and S. Chen, *Nanoscale Horiz.*, 2020, **5**, 488–494.
22 L. Ming, I. Zabala-Gutierrez, P. Rodríguez-Sevilla, J. R. Retama, D. Jaque, R. Marin and E. Ximendes, *Adv. Mater.*, 2023, **35**, 2306606.
23 C. D. S Brites, A. Millán and L. D. Carlos, *Handb. Phys. Chem. Rare Earths*, 2016, **49**, 339–427.
24 C. D. S. Brites, S. Balabhadra and L. D. Carlos, *Adv. Opt. Mater.*, 2019, **7**, 1801239.
25 M. Dai, B. Zhou and D. Yan, *Angew. Chem., Int. Ed.*, 2025, **64**, e202505322.
26 P. Li, Z. Qi and D. Yan, *Angew. Chem., Int. Ed.*, 2024, **63**, e202411000.
27 M. K. Johansson, R. M. Cook, J. Xu and K. N. Raymond, *J. Am. Chem. Soc.*, 2004, **126**, 16451–16455.
28 J. C. G. Bünzli and C. Piguet, *Chem. Soc. Rev.*, 2005, **34**, 1048–1077.
29 Y. Cui, H. Xu, Y. Yue, Z. Guo, J. Yu, Z. Chen, J. Gao, Y. Yang, G. Qian and B. Chen, *J. Am. Chem. Soc.*, 2012, **134**, 3979–3982.
30 X. Rao, T. Song, J. Gao, Y. Cui, Y. Yang, C. Wu, B. Chen and G. Qian, *J. Am. Chem. Soc.*, 2013, **135**, 15559–15564.
31 Y. Cui, R. Song, J. Yu, M. Liu, Z. Wang, C. Wu, Y. Yang, Z. Wang, B. Chen and G. Qian, *Adv. Mater.*, 2015, **27**, 1420–1425.
32 K. Miyata, Y. Konno, T. Nakanishi, A. Kobayashi, M. Kato, K. Fushimi and Y. Hasegawa, *Angew. Chem., Int. Ed.*, 2013, **52**, 6413–6416.
33 H. Yan, C. M. S. Calado, H. Wang, M. Murugesu and W.-B. Sun, *Chem. Sci.*, 2025, **16**, 4821–4830.
34 J. Wang, J. J. Zakrzewski, M. Zychowicz, V. Vieru, L. F. Chibotaru, K. Nakabayashi, S. Chorazy and S. Ohkoshi, *Chem. Sci.*, 2021, **12**, 730–741.
35 D. Ananias, F. A. Almeida Paz, D. S. Yufit, L. D. Carlos and J. Rocha, *J. Am. Chem. Soc.*, 2015, **137**, 3051–3058.
36 H. Guan, M. Qi, L. Shi, W. Liu, L. Yang and W. Dou, *ACS Appl. Mater. Interfaces*, 2023, **15**, 18114–18124.
37 D. Errulat, R. Marin, D. A. Gálico, K. L. M. Harriman, A. Pialat, B. Gabidullin, F. Iikawa, O. D. D. Couto Jr, J. O. Moilanen, E. Hemmer, F. A. Sigoli and M. Murugesu, *ACS Cent. Sci.*, 2019, **5**, 1187–1198.
38 J. Wang, J. J. Zakrzewski, M. Zychowicz, Y. Xin, H. Tokoro, S. Chorazy and S.-I. Ohkoshi, *Angew. Chem., Int. Ed.*, 2023, **62**, e202306372.
39 G.-C. Bao, K.-L. Wong, D. Jin and P. A. Tanner, *Light:Sci. Appl.*, 2018, **7**, 96.
40 K. A. Romanova, A. Y. Freidzon, A. A. Bagaturyants and Y. G. Galyametdinov, *J. Phys. Chem. A*, 2014, **118**, 11244–11252.

41 L. Liang, X. Yang, X. Yan, Y. Kou, Y. Zhang, P. Su and Y. Tang, *Adv. Mater.*, 2025, **38**, e14252.
42 Y. Yang, K.-Z. Wang and D. Yan, *ACS Appl. Mater. Interfaces*, 2017, **9**, 17399.
43 Y. Yang, K.-Z. Wang and D. Yan, *Chem. Commun.*, 2017, **53**, 7752.
44 R. Gao, M. Zhao, Y. Guan, X. Fang, X. Li and D. Yan, *J. Mater. Chem. C*, 2014, **2**, 9579.
45 A. Khatkar, A. Khatkar and A. Chauhan, *J. Mater. Sci.*, 2024, **59**, 15048–15076.
46 P. Jiang and Z. Guo, *Coord. Chem. Rev.*, 2004, **248**, 205–229.
47 Y. Cui, F. Zhu, B. Chen and G. Qian, *Chem. Commun.*, 2015, **51**, 7420–7431.
48 L. H. Fischer, G. S. Harms and O. S. Wolfbeis, *Angew. Chem., Int. Ed.*, 2011, **50**, 4546–4551.
49 E. C. Ximendes, W. Q. Santos, U. Rocha, U. K. Kagola, F. SanzRodríguez, N. Fernández, A. d. S. Gouveia-Neto, D. Bravo, A. M. Domingo, B. del Rosal, C. D. S. Brites, L. D. Carlos, D. Jaque and C. Jacinto, *Nano Lett.*, 2016, **16**, 1695–1703.
50 L. Shi, W. Song, C. Lian, W. Chen, J. Mei, J. Su, H. Liu and H. Tian, *Adv. Opt. Mater.*, 2018, **6**, 1800190–1800198.
51 D. Zhao, D. Yue, K. Jiang, Y. Cui, Q. Zhang, Y. Yang and G. Qian, *J. Mater. Chem. C*, 2017, **5**, 1607–1613.
52 Y. Ding, Y. Lu, K. Yu, S. Wang, D. Zhao and B. Chen, *Adv. Opt. Mater.*, 2021, **9**, 2100945–2100953.
53 (*a*) CCDC 2270399: Experimental Crystal Structure Determination, 2026, DOI: 10.5517/ccdc.csd.cc2g6jpx; (*b*) CCDC 2503173: Experimental Crystal Structure Determination, 2026, DOI: 10.5517/ccdc.csd.cc2q0rj1.